MNRAS **000**, 1–13 (2022) Preprint 30 November 2022 Compiled using MNRAS LATEX style file v3.0

Constraints on local primordial non-Gaussianity from the large-scale clustering of DESI Luminous Red Galaxies

Mehdi Rezaie[1,2], Ashley J. Ross[3], Hee-Jong Seo[2], Hui Kong[3], Edmond Chaussidon[4], Anna Porredon[3], Lado Samushia[1], Rongpu Zhou[5], Alex Krolewski[6,7,8], Arnaud de Mattia[4], Jose Bermejo[?], Florian Beutler[9], Christophe Yeche[4], Nathalie Palanque-Delabrouille[4,5], Klaus Honscheid[3,10], and DESI Members

[1]*Department of Physics, Kansas State University, 116 Cardwell Hall, Manhattan, KS 66506, USA*
[2]*Department of Physics and Astronomy, Ohio University, Athens, OH 45701, USA*
[3]*Center for Cosmology and AstroParticle Physics, The Ohio State University, 191 West Woodruff Avenue, Columbus, OH 43210, USA*
[4]*IRFU, CEA, Universite Paris-Saclay, F-91191 Gif-sur-Yvette, France*
[5]*Lawrence Berkeley National Laboratory, 1 Cyclotron Road, Berkeley, CA 94720, USA*
[6]*Department of Physics and Astronomy, University of Waterloo, 200 University Ave W, Waterloo, ON N2L 3G1, Canada*
[7]*Perimeter Institute for Theoretical Physics, 31 Caroline St. North, Waterloo, ON N2L 2Y5, Canada*
[8]*Waterloo Centre for Astrophysics, University of Waterloo, 200 University Ave W, Waterloo, ON N2L 3G1, Canada*
[9]*Institute for Astronomy, University of Edinburgh, Royal Observatory, Blackford Hill, Edinburgh EH9 3HJ, UK*
[10]*Department of Physics, The Ohio State University, 191 West Woodruff Avenue, Columbus, OH 43210, USA*

Accepted XXX. Received YYY; in original form ZZZ

ABSTRACT

This paper uses the large-scale clustering of luminous red galaxies selected from the Dark Energy Spectroscopic Instrument Legacy Imaging Surveys Data Release 9 to constrain the local primordial non-Gaussianity (PNG) parameter $f_{\rm NL}$. Using the angular power spectrum, we thoroughly investigate the impact of various photometric systematic effects, such as those caused by Galactic extinction and varying survey depth. Simulations are utilized to construct covariance matrices, evaluate the robustness of our pipeline, and perform statistical tests to assess whether spurious fluctuations are properly mitigated and calibrated. Using modes from $\ell = 2$ to 300, we find $X1 < f_{\rm NL} < X2$ with our conservative and $X1 < f_{\rm NL} < X2$ with extreme treatment of imaging systematics, both at 68% confidence. While our results are consistent with zero PNG, but we show that the understanding of imaging systematics is of paramount importance to obtain unbiased constraints on $f_{\rm NL}$.

Key words: cosmology: inflation - large-scale structure of the Universe

1 INTRODUCTION

Current observations of the cosmic microwave background (CMB), large-scale structure (LSS), and supernovae (SN) are explained by a cosmological model that consists of dark energy, dark matter, and ordinary luminous matter, which has gone through a phase of rapid expansion, known as *inflation*, at its early stages (see, e.g., Weinberg et al. 2013). The theory of inflation elegantly addresses fundamental issues with the hot Big Bang theory, such as the isotropy of the CMB temperature, absence of magnetic monopole, and flatness of the Universe. At the end of inflation, the Universe was reheated and primordial fluctuations are generated to seed the subsequent growth of structure. While the presence of an inflationary era is certain but the details of the inflation field still remain highly unknown, and statistical properties of primordial fluctuations pose as one of the puzzling questions in modern observational cosmology. Analyses of cosmological data have revealed that initial conditions of the Universe are consistent with Gaussian fluctuations; however, there are some classes of models that predict some levels of non-Gaussianities in the primordial gravitational field. In its simplest form, primordial non-Gaussianity depends on the local value of the gravitational potential ϕ and is parameterized by a nonlinear parameter $f_{\rm NL}$ (Komatsu & Spergel 2001),

$$\Phi = \phi + f_{\rm NL}[\phi^2 - <\phi^2>]. \qquad (1)$$

Standard slow roll inflation predicts $f_{\rm NL}$ to be of order 10^{-2}, while multifield theories predict considerably higher values than unity. Therefore, a robust measurement of $f_{\rm NL}$ can be considered as the first stepping stone toward better understanding the physics of the early Universe.

Current tightest bound on $f_{\rm NL}$ comes from the three-point clustering analysis of the CMB temperature anisotropies by the Planck satellite, $f_{\rm NL} = 0.9 \pm 5.0$ (Akrami et al. 2019). CMB S4, next generation of CMB experiments, will improve this constraint but since CMB is limited by cosmic variance, it alone cannot further enhance to break the degeneracy amongst inflationary models. However, combining CMB with LSS data could cancel cosmic variance, partially if not completely, and enhance these limits to a precision level required to differentiate between various inflationary models (see, e.g., Schmittfull & Seljak 2018).

PNG alters local number density of galaxies by coupling the long and small wavelength modes of dark matter gravitational field, and as a result it introduces a k^{-2}-dependent shift in halo bias which leaves its signature on the large scales in the two-point clustering of galaxies and quasars (see, e.g., Dalal et al. 2008). Measuring $f_{\rm NL}$ using the scale-dependent bias is however very challenging due to the presence of observational systematic effects which cause excess clustering signal on the same scales sensitive to $f_{\rm NL}$. Previous studies with galaxy and quasar clustering have been hindered dramatically by spurious fluctuations in target density, which are due to the variation of imaging properties across the sky (Ho et al. 2015). For instance, Pullen & Hirata (2013) found that the level of systematic contamination in the quasar sample of SDSS DRX does not allow a robust $f_{\rm NL}$ measurement. These imaging systematic issues are expected to be severe for wide-area galaxy surveys that observe the night sky closer to the Galactic plane and attempt to relax the selection criteria to include fainter targets. Assuming imaging systematics are under control, the next generation of galaxy surveys such as DESI and the Rubin Observatory are forecast to yield unprecedented constraints on $f_{\rm NL}$.

In this paper, we use the photometric sample of luminous red galaxies (LRGs) from the DESI Legacy Imaging Surveys Data Release 9, hereafter referred to as DR9, to constrain the local primordial non-Gaussianity parameter $f_{\rm NL}$, while testing the robustness of our results against various sources of systematic effects. We also make use of spectroscopic data from DESI Survey Validation to determine the redshift distribution of galaxies. We cross correlate the DR9 density field with the templates of imaging realities to assess the effectiveness of treatment methods and to characterize the significance of residual systematic error. Section 2 describes the DR9 sample and simulations with and without PNG and imaging systematic effects, and Section 3 outlines the theory for modeling angular power spectrum and analysis techniques for quantifying various observational systematic effects. Finally, we present the results in Section 4, and conclude with a comparison to previous $f_{\rm NL}$ constraints in Section 5.

2 DATA

Luminous red galaxies (LRGs) are massive galaxies that lack active star formation and considered as one of the highly biased tracers of large scale structure. LRGs have a simple color-magnitude selection due to a break around 4000 Å in their spectra. They are widely targeted in previous galaxy redshift surveys CITE, and their clustering and redshift properties are well studied CITE.

We use LRGs selected from the DESI Imaging Surveys Data Release 9 (Dey et al. 2018) using color-magnitude cuts described in the g, r, z bands in the optical and $W1$ band in the infrared. The selection is described in detail in Zhou et al. (2021), and summarized in Tab. 1.The DR9 sample is masked for bright stars, foreground

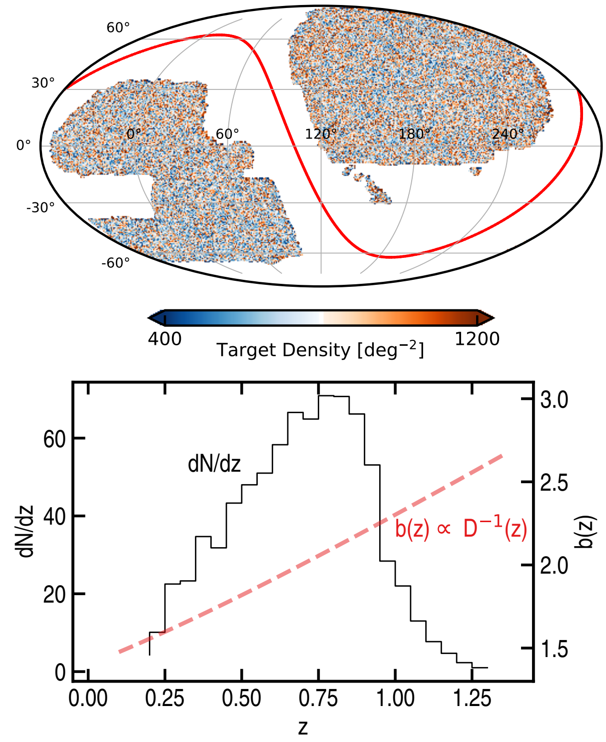

Figure 1. Top: Observed density field of DESI Luminous Red Galaxies Data Release 9 in deg^{-2}. Spurious disconnected islands from the DECaLS North footprint at Declination below -11 and parts of the DECaLS South with Declination below -30 are dropped from the DR9 sample due to potential calibration issues. Bottom: Redshift distribution and bias evolution of DESI LRGs. The redshift distribution is deducted from spectroscopy and the bias model assumes a constant clustering amplitude.

bright galaxies as well as clusters of galaxies[1], and then binned into HEALPIX (Gorski et al. 2005) at NSIDE = 256 to construct the LRG density field, with an average density of 800 deg^{-2} with a coverage around 14000 square degrees of the sky. Fig. 1 shows observed density field of DR9 LRGs in deg^{-2}. There are some disconnected islands, hereafter referred to as *spurious islands*, in the DECaLS North region at Declination below -11, which are removed from the sample to minimize potential calibration issues. Additionally, parts of the DECaLS South with Declination below -30 are cut from the sample, since similar calibration issues might infect our analysis. Section 4 presents how these cuts might alter constraints. DESI imaging is a multi-epoch dataset, and thus LRG density map is accounted for pixel incompleteness using a catalog of random points, uniformly scattered over the footprint with the same cuts and masks as DR9 LRGs. Fig. 1 shows the redshift distribution of DR9 LRGs inferred from DESI Survey Validation CITE and the evolution of galaxy bias for our LRG sample adapted from Zhou et al. (2021), consistent with the assumption of constant clustering amplitude.

We study the correlation coefficient between the LRG density map and potential sources of systematic error, mapped into HEALPIX at the same NSIDE. The maps used in this work are local stellar density constructed from point-like sources with a g-band magnitude in the range $12 \leq g < 17$ from Gaia Data Release 2 (see, Gaia Collaboration et al. 2018; Myers et al. 2022), Galactic

[1] See `https://www.legacysurvey.org/dr9/bitmasks/`

Table 1. Selection criteria for the LRG targets.

Footprint	Criterion	Description
DECaLS	$z_{\rm fiber} < 21.7$	Faint limit
	$z - W1 > 0.8 \times (r - z) - 0.6$	Stellar rejection
	$[(g - r > 1.3)$ AND $((g - r) > -1.55 * (r - W1) + 3.13)]$ OR $(r - W1 > 1.8)$	Remove low-z galaxies
	$[(r - W1 > (W1 - 17.26) * 1.8)$ AND $(r - W1 > W1 - 16.36)]$ OR $(r - W1 > 3.29)$	Luminosity cut
BASS+MzLS	$z_{\rm fiber} < 21.71$	Faint limit
	$z - W1 > 0.8 \times (r - z) - 0.6$	Stellar rejection
	$[(g - r > 1.34)$ AND $((g - r) > -1.55 * (r - W1) + 3.23)]$ OR $(r - W1 > 1.8)$	Remove low-z galaxies
	$[(r - W1 > (W1 - 17.24) * 1.83)$ AND $(r - W1 > W1 - 16.33)]$ OR $(r - W1 > 3.39)$	Luminosity cut

extinction E[B-V] from Schlegel et al. (1998), and other imaging properties including survey depth (galaxy depth in grz and PSF depth in W1) and seeing in grz from DESI imaging. Fig. 3 shows the Spearman correlation between galaxy density and imaging properties.

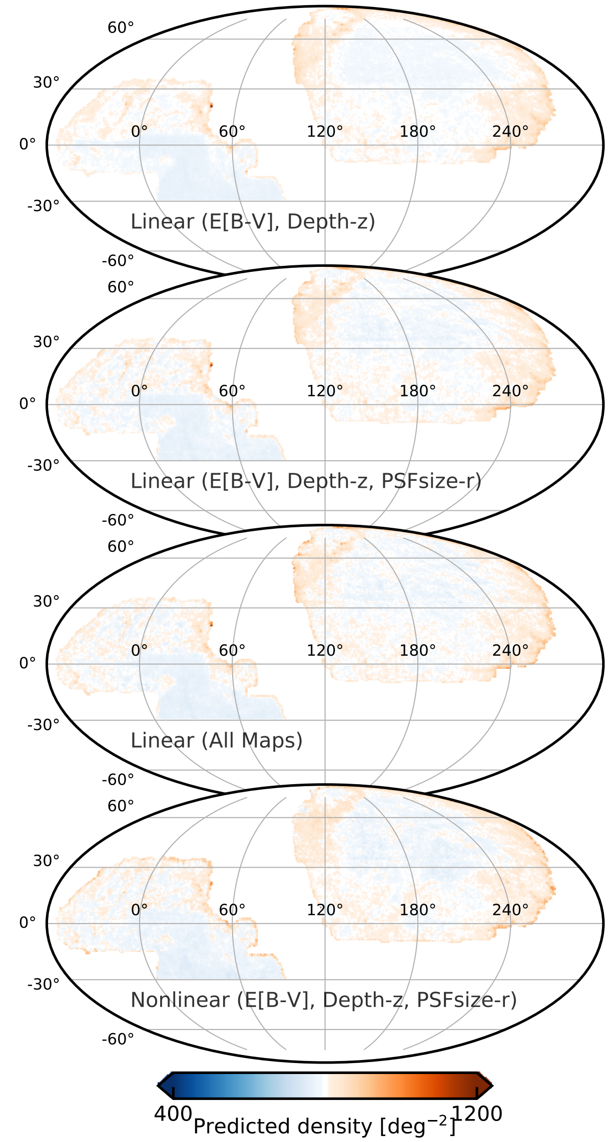

Figure 2. Predicted galaxy counts from template regression. Baseline approach uses imaging maps from Zhou et al. (2022): EBV, galaxy depth in rgz, psfdepth in W1, and psfsize in grz. Conservative I uses EBV and galaxy depth in z, and Conservative II uses EBV, galaxy depth in z, and psfsize in r. In all approaches, the models are regressed on BASS+MzLS, DECaLS North, and DECaLS South separately.

3 METHODOLOGY

3.1 Measuring Power Spectrum

Galaxy density contrast in pixel i is defined as,

$$\hat{\delta}_i = \frac{\rho_i}{\hat{\bar{\rho}}} - 1, \tag{2}$$

where ρ is the density of galaxies accounted for pixel area $f_{{\rm pix},i}$ and $\hat{\bar{\rho}}$ is the mean galaxy density estimated by,

$$\hat{\bar{\rho}} = \frac{\sum_i \rho_i f_{{\rm pix},i}}{\sum_i f_{{\rm pix},i}}. \tag{3}$$

By definition, Eqs. 2 and 3 ensure that the integral of the observed quantity over the footprint vanishes:

$$\sum_i \hat{\delta}_i \, f_{{\rm pix},i} = 0, \tag{4}$$

To estimate power spectrum, we expand the galaxy overdensity field in terms of Legendre polynomials,

$$\hat{\delta}_i = \sum_{\ell=0}^{\ell_{\rm max}} \sum_{m=-\ell}^{\ell} a_{\ell m} Y_{\ell m}(\theta_i, \phi_i), \tag{5}$$

where θ, ϕ represent the polar and azimuthal angular coordinates of pixel i, respectively. The cutoff at $\ell = \ell_{\rm max}$ assumes that modes with $\ell > \ell_{\rm max}$ do not contribute significantly to signal power. The coefficients $a_{\ell m}$ are then obtained by integrating the density contrast field over the total number of non-empty pixels $N_{\rm pix}$ and using the orthogonality of Legendre polynomials:

$$\hat{a}_{\ell m} = \frac{4\pi}{N_{\rm pix}} \sum_{i=1}^{N_{\rm pix}} \hat{\delta}_i \, f_{{\rm pix},i} \, Y^*_{\ell m}(\theta_i, \phi_i), \tag{6}$$

where * represents the complex conjugate. Then, the angular power spectrum estimator is defined as the variance of $\hat{a}_{\ell m}$ coefficients:

$$\hat{C}_\ell = \frac{1}{2\ell + 1} \sum_{m=-\ell}^{\ell} \hat{a}_{\ell m} \hat{a}^*_{\ell m}. \tag{7}$$

In order to extract $\hat{a}_{\ell m}$ and compute the angular power spectrum, C_ℓ, we make use of the ANAFAST function from HEALPix (Gorski et al. 2005) with the third order iteration of the quadrature

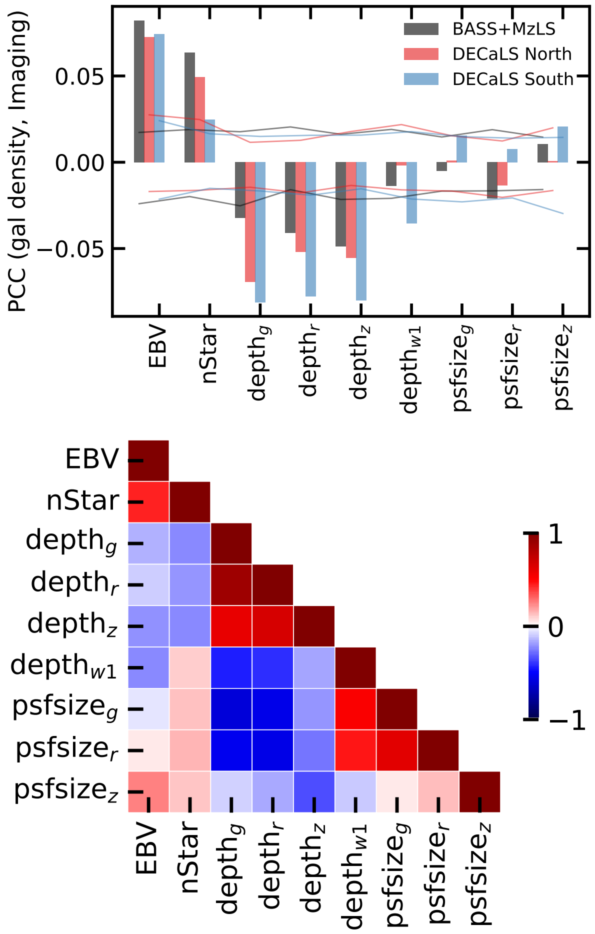

Figure 3. Top: Pearson-r correlation coefficient between galaxy density and imaging properties in the three imaging regions (top) and between imaging properties themselves for the full DESI footprint (bottom). Solid curves represent the range of correlations observed in 100 randomly selected mock realizations.

to increase the accuracy[2]. Due to the survey geometry implicit in the summation over the non-empty pixels and explicit in $f_{\rm pix,i}$, our estimator does not return an unbiased estimate of power spectrum, and thus the same effect must be accounted in the modeling of power spectrum. We ignore $\ell = 0$ and 2 and bin spectra with $\Delta\ell = 10$ up to $\ell_{\rm max}$ =

3.2 Modeling Power Spectrum

The projected angular power spectrum of galaxies in the presence of redshift space distortions and local primordial non-Gaussianity is related to the 3D linear power spectrum $P(k)$ and shotnoise $N_{\rm shot}$ by (see, e.g., Slosar et al. 2008),

$$C_\ell = \frac{2}{\pi}\int_0^\infty \frac{dk}{k}k^3 P(k)|\Delta_\ell(k)|^2 + N_{\rm shot}, \tag{8}$$

where $\Delta_\ell(k) = \Delta_\ell^{\rm g}(k) + \Delta_\ell^{\rm RSD}(k) + \Delta_\ell^{\rm f_{NL}}(k)$ and,

$$\Delta_\ell^{\rm g}(k) = \int \frac{dr}{r} r b(r) D(r) \frac{dN}{dr} j_\ell(kr), \tag{9}$$

$$\Delta_\ell^{\rm RSD}(k) = -\int \frac{dr}{r} r f(r) D(r) \frac{dN}{dr} j_\ell''(kr), \tag{10}$$

$$\Delta_\ell^{\rm f_{NL}}(k) = f_{\rm NL}\frac{\alpha}{k^2 T(k)}\int \frac{dr}{r} r[b(r)-p]\frac{dN}{dr} j_\ell(kr), \tag{11}$$

where $\alpha = 3\delta_c\Omega_M(H_0/c)^2$, $b(r)$ is the linear bias, dN/dr is the normalized redshift distribution of galaxies[3], $D(r)$ is the normalized growth factor such that $D(0) = 1$, $f(r)$ is the growth rate, and r is the comoving distance. The parameter p is the response of the tracer to halo's gravitational field, e.g., 1 for luminous red galaxies and 1.6 for recent mergers. In order to overcome rapid oscillations in spherical Bessel functions, we employ the FFTLog[4] algorithm and its extension as implemented in **?** to compute the inner integrations over $d\ln r$.

3.2.1 *Survey Geometry*

For a galaxy survey that observes the sky partially, the measured power spectrum is convolved with the survey geometry. This means that the pseudo-power spectrum $\hat{C}_\ell$ obtained by the direct Spherical Harmonic Transforms of a partial sky map, differs from the full-sky angular spectrum C_ℓ. However, their ensemble average is related by (**?**)

$$< \hat{C}_\ell > = \sum_{\ell'} M_{\ell\ell'} < C_{\ell'} >, \tag{12}$$

where $M_{\ell\ell'}$ represents the mode-mode coupling from the partial sky coverage. This is known as the Window Function effect and a proper assessment of this effect is crucial for a robust measurement of the large-scale clustering of galaxies. This window effect is a source of observational systematic error and impacts the measured galaxy clustering, especially on scales comparable to survey size.

We follow a similar approach to that of (**?**) to model the window function effect on the theoretical power spectrum C_ℓ rather than correcting the measured pseudo-power spectrum from data. First, we use HEALPIX to compute the pseudo-power spectrum of the window $\hat{C}_\ell^{\rm window}$, which is defined by a mask file in ring ordering format with NSIDE= 256. Then, we transform it to correlation function by,

$$\omega^{\rm window}(\theta) = \frac{1}{4\pi}\sum_\ell (2\ell+1)\hat{C}_\ell^{\rm window} P_\ell(\cos\theta). \tag{13}$$

Next, we normalize $\omega^{\rm window}$ such that it is normalized to one at $\theta = 0$. Finally, we multiply the theory correlation function by $\omega^{\rm window}$ and transform the result back to ℓ-space,

$$\hat{\omega}^{\rm model} = \omega^{\rm model}\omega^{\rm window} \tag{14}$$

$$\hat{C}_\ell^{\rm model} = 2\pi\int d\theta\, \hat{\omega}^{\rm model}(\theta) P_\ell(\cos\theta). \tag{15}$$

[2] We refer the reader to https://healpix.sourceforge.io/pdf/subroutines.pdf, p. 104-105.

[3] $dN/dr = (dN/dz) * (dz/dr) \propto (dN/dz) * H(z)$

[4] github.com/xfangcosmo/FFTLog-and-beyond

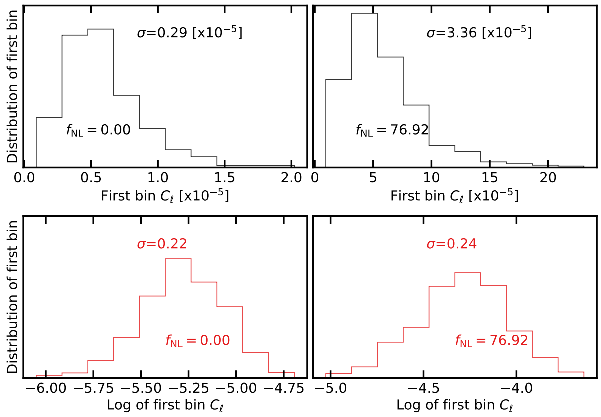

Figure 4. Distribution of the first bin power spectrum for $f_{\rm NL}$ = 0 and 100 mocks.

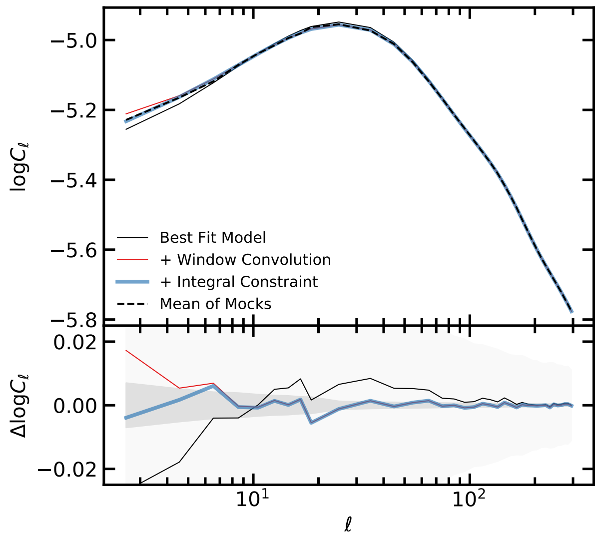

Figure 5. Mean power spectrum of 1000 mocks with $f_{\rm NL}$ = 0 and best fit theoretical prediction after accounting for various theoretical systematic effects.

3.2.2 *Integral Constraint*

The integral of the galaxy density contrast δ on the footprint is bound to zero, which is often referred to as the *Integral Constraint*. We account for this effect in the modeling by,

$$\hat{C}_{\ell}^{\rm model, IC} = \hat{C}_{\ell}^{\rm model} - \hat{C}_{\ell=0}^{\rm model}\left(\frac{\hat{C}_{\ell}^{\rm window}}{\hat{C}_{\ell=0}^{\rm window}}\right) \tag{16}$$

3.3 Characterization of systematic effects

We use the diagnostic tests presented in Rezaie et al 2021 based on cross power spectrum between galaxy density field and imaging maps and mean density contrast as a function of imaging properties to quantify the significance of imaging systematic effects.

3.3.1 *Cross Spectrum*

Taking $C_{\ell}^{g,x}$ as the cross power spectrum between galaxy density contrast field and imaging map, one can normalize this quantity by auto power spectrum of imaging map itself:

$$\hat{C}_{x,\ell} = \frac{(\hat{C}_{\ell}^{g,x})^2}{\hat{C}_{\ell}^{x,x}}, \tag{17}$$

and then construct a vector from cross spectra against all other imaging maps:

$$\hat{C}_{X,\ell} = [\hat{C}_{x_1,\ell}, \hat{C}_{x_2,\ell}, \hat{C}_{x_3,\ell}, ..., \hat{C}_{x_9,\ell}]. \tag{18}$$

We bin the C_X measurements with ℓ edges defined at $2, 10, 18, 26, 40, 60, 80,$ and 100. The mean and standard deviation of $\hat{C}_{X,\ell}$ for 1000 mocks with and without $f_{\rm NL}$ are shown in Fig. 6. Finally, cross power spectrum χ^2 can be defined as,

$$\chi^2 = C_{X,\ell}^{T} C^{-1} C_{X,\ell}, \tag{19}$$

where covariance matrix $C = < C_{X,\ell} C_{X,\ell'} >$ is constructed from mocks without systematic effects. This statistics is measured for every mock realization with the leave-one-out technique to construct a histogram, which is then compared to the χ^2 value observed from the DR9.

3.3.2 *Mean Density*

As an alternative test, we calculate the histogram of the density contrast field relative to each imaging map.

$$\delta_x = (\hat{\bar{\rho}})^{-1} \frac{\sum_i \rho_i f_{{\rm pix},i}}{\sum_i f_{{\rm pix},i}}, \tag{20}$$

where the summations are over pixels in each bin of imaging map x. Similarly, we construct the mean density contract vector against all imaging maps,

$$\delta_X = [\delta_{x_1}, \delta_{x_2}, \delta_{x_3}, ..., \delta_{x_9}], \tag{21}$$

and the total residual error as,

$$\chi^2 = \delta_X^T C^{-1} \delta_X, \tag{22}$$

where the covariance matrix $C = < \delta_X \delta_X >$ is constructed from mocks without systematic effects. Fig. 6 shows the cross power spectrum and mean density contrast for the DR9 LRG sample. The shades represent the 1σ level fluctuations observed in 1000 clean mocks with $f_{\rm NL}$ = 0 and 100.

4 RESULTS

TODO: The mean density and cross power spectrum χ^2 diagnostics do not reveal any signature of remaining systematic effects – given all the available templates. But we could be missing some unknown maps. There are some calibration maps made by Aaron which I need to look into. I did not use the Gaia stellar map for training– Zhou et al has a discussion on why it should not be used. But I plan to apply some cuts based on imaging (e.g., poor depth, high stellar density and extinction) to see if those impact the best fit estimates. Next, I will study how changing the lowest ell used could affect our results.

4.1 Lognormal Mocks

Corner plots of the PNG parameter $f_{\rm NL}$ and bias coefficient are shown in Fig. 8 for fitting the mean power spectrum of the mocks, with and without $f_{\rm NL}$. Maximum-A-Posteriori estimates and marginalized mean, median and 1σ quantiles are summarized

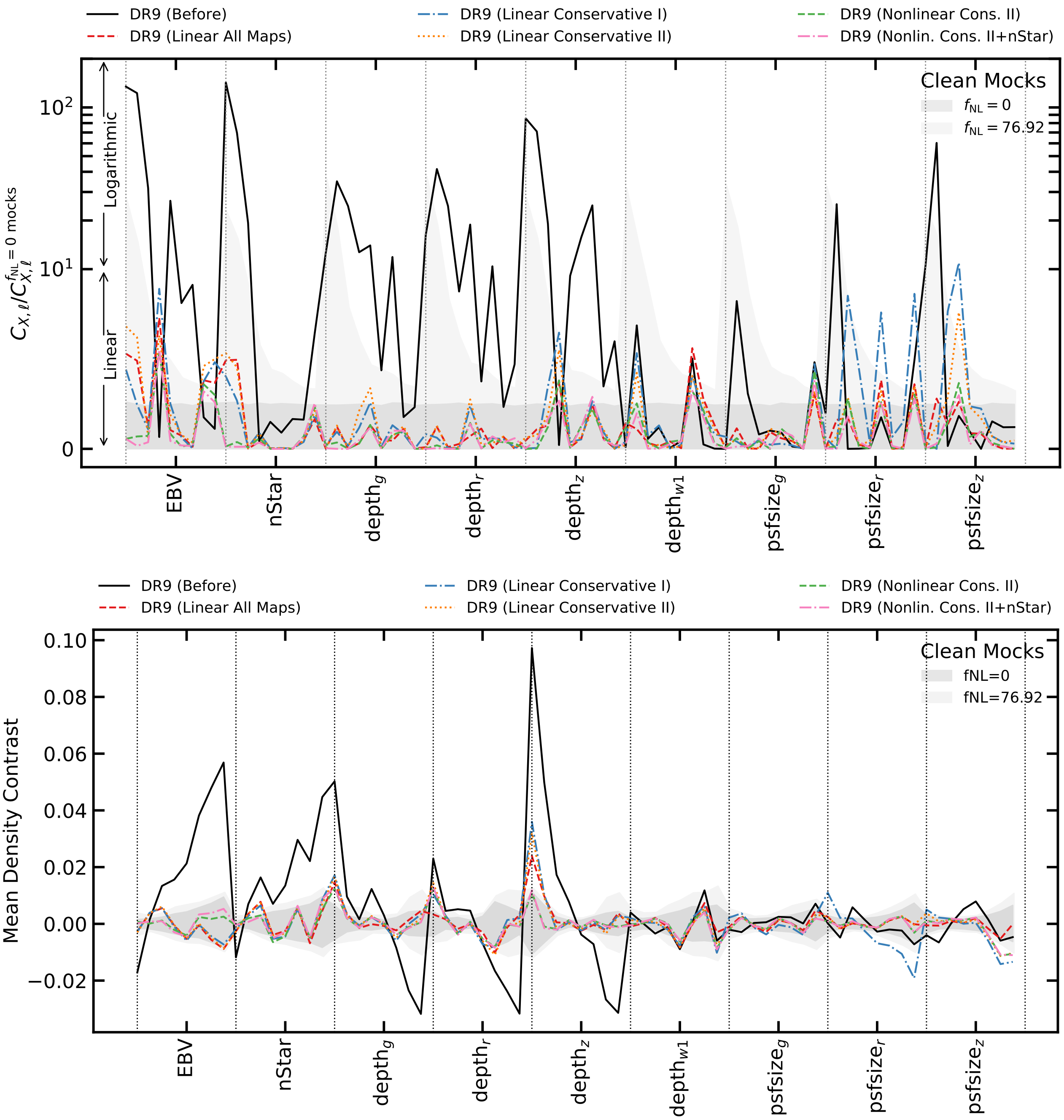

Figure 6. Residual systematic fluctuations of DR9 LRGs against imaging maps. Left: cross spectrum. Right: mean density contrast. Shades represent 1σ dispersion of 1000 clean mocks with and without $f_{\rm NL}$.

in Tab. 2. Comparing DECaLS North with sky coverage 0.14 to full DESI with 0.40, we find the constraint improve by a factor of 1.9 which is slightly more than $\sim f_{\rm SKY}^{-1/2}$, 1.7. while As a robustness test, we also fit the mean power spectrum of the $f_{\rm NL}=100$ mocks using the covariance matrix estimated from the $f_{\rm NL}=0$ mocks. We find that the constraints improve by a factor of 4.2, due to a higher signal to noise ratio.

4.2 DR9 LRGs

5 CONCLUSION

ACKNOWLEDGEMENTS

DATA AVAILABILITY

REFERENCES

Akrami Y., et al., 2019, arXiv preprint arXiv:1905.05697
Dalal N., Dore O., Huterer D., Shirokov A., 2008, Physical Review D, 77, 123514
Dey A., et al., 2018, arXiv preprint arXiv:1804.08657

Table 2. Maximum-A-Posteriori (MAP) and marginalized mean estimates for $f_{\rm NL}$ from fitting the mean power spectrum of the mocks. Degree of freedom is 34 (37 data points - 3 parameters).

			$f_{\rm NL}$				
True $f_{\rm NL}$	Footprint	Observable	Best fit	Mean	68% CL	95% CL	χ^2
76.92	DESI	$\log C_\ell$	77.67	77.67	$77.17 < f_{\rm NL} < 78.16$	$76.71 < f_{\rm NL} < 78.64$	38.8
76.92	DESI	C_ℓ	77.67	77.65	$77.17 < f_{\rm NL} < 78.14$	$76.70 < f_{\rm NL} < 78.60$	39.0
76.92	DESI	$\log C_\ell$ + $f_{\rm NL} = 0$ cov	77.70	77.71	$77.25 < f_{\rm NL} < 78.17$	$76.81 < f_{\rm NL} < 78.63$	39.9
76.92	DESI	C_ℓ + $f_{\rm NL} = 0$ cov	77.03	77.02	$76.93 < f_{\rm NL} < 77.12$	$76.83 < f_{\rm NL} < 77.22$	207.6
0	DESI	$\log C_\ell$	0.36	0.36	$0.06 < f_{\rm NL} < 0.65$	$-0.23 < f_{\rm NL} < 0.94$	35.7
0	DECaLS North	$\log C_\ell$	0.07	0.06	$-0.47 < f_{\rm NL} < 0.60$	$-1.00 < f_{\rm NL} < 1.12$	26.7
0	DECaLS South	$\log C_\ell$	0.67	0.67	$0.13 < f_{\rm NL} < 1.22$	$-0.40 < f_{\rm NL} < 1.75$	34.3
0	BASS+MzLS	$\log C_\ell$	0.83	0.82	$0.25 < f_{\rm NL} < 1.40$	$-0.31 < f_{\rm NL} < 1.96$	39.4

Table 3. Best fit and marginalized estimates for $f_{\rm NL}$ from fitting the mean power spectrum of the mocks before and after applying imaging weights.

			$f_{\rm NL}$			
Mock	Method	Best fit	Mean	68% CL	95% CL	χ^2
0	No Weight	0.36	0.36	$0.06 < f_{\rm NL} < 0.65$	$-0.23 < f_{\rm NL} < 0.94$	35.7
0	ConsII	−11.64	−11.65	$-12.00 < f_{\rm NL} < -11.30$	$-12.34 < f_{\rm NL} < -10.97$	86.8
0	ConsII+nStar	−20.14	−20.13	$-20.44 < f_{\rm NL} < -19.82$	$-20.74 < f_{\rm NL} < -19.52$	472.8
Contaminated 0	ConsII	−12.12	−12.13	$-12.48 < f_{\rm NL} < -11.78$	$-12.83 < f_{\rm NL} < -11.44$	94.0
Contaminated 0	ConsII+nStar	−20.97	−20.98	$-21.28 < f_{\rm NL} < -20.67$	$-21.58 < f_{\rm NL} < -20.37$	556.3
76.92	No Weight	77.67	77.67	$77.17 < f_{\rm NL} < 78.16$	$76.71 < f_{\rm NL} < 78.64$	38.8
76.92	ConsII	54.57	54.57	$54.14 < f_{\rm NL} < 55.01$	$53.72 < f_{\rm NL} < 55.45$	603.5
76.92	ConsII+nStar	38.38	38.38	$37.99 < f_{\rm NL} < 38.78$	$37.60 < f_{\rm NL} < 39.16$	537.0
Contaminated 76.92	ConsII	54.01	54.00	$53.57 < f_{\rm NL} < 54.44$	$53.15 < f_{\rm NL} < 54.86$	588.0
Contaminated 76.92	ConsII+nStar	37.48	37.49	$37.09 < f_{\rm NL} < 37.88$	$36.70 < f_{\rm NL} < 38.27$	510.7

Table 4. Maximum-A-Posteriori (MAP) and marginalized mean estimates for $f_{\rm NL}$ from fitting power spectrum of DR9 LRGs before and after correcting for systematics. Degree of freedom is 34 (37 data points - 3 parameters).

			$f_{\rm NL}$			
Footprint	Method	Best fit	Mean	68% CL	95% CL	χ^2
DESI	No Weight	113.18	115.49	$98.14 < f_{\rm NL} < 132.89$	$83.51 < f_{\rm NL} < 151.59$	44.4
DESI	Linear (All Maps)	36.05	37.72	$26.13 < f_{\rm NL} < 49.21$	$16.31 < f_{\rm NL} < 62.31$	41.1
DESI	Linear (Conservative I)	49.58	51.30	$38.21 < f_{\rm NL} < 64.33$	$27.41 < f_{\rm NL} < 78.91$	38.8
DESI	Linear (Conservative II)	36.63	38.11	$26.32 < f_{\rm NL} < 49.86$	$16.36 < f_{\rm NL} < 63.12$	39.6
DESI	Nonlinear (Cons. II)	28.58	29.79	$18.91 < f_{\rm NL} < 40.59$	$9.47 < f_{\rm NL} < 52.73$	34.6
DESI	Nonlin. (Cons. II+nStar)	16.63	17.52	$7.51 < f_{\rm NL} < 27.53$	$-1.59 < f_{\rm NL} < 38.49$	35.2
DESI	Nonlin. (All Maps+nStar)	−5.87	−9.19	$-21.45 < f_{\rm NL} < 2.40$	$-33.81 < f_{\rm NL} < 12.06$	39.5
DESI (imag. cut)	Nonlin. (Cons. II)	29.16	30.57	$19.05 < f_{\rm NL} < 42.18$	$9.01 < f_{\rm NL} < 54.81$	35.8
DESI (comp. cut)	Nonlin. (Cons. II)	28.07	29.48	$18.38 < f_{\rm NL} < 40.50$	$8.81 < f_{\rm NL} < 53.10$	34.5
DESI	Nonlin. (Cons. II)+$f_{\rm NL} = 76.92$ Cov	31.62	33.11	$20.94 < f_{\rm NL} < 45.24$	$10.56 < f_{\rm NL} < 59.16$	33.5
BASS+MzLS	Nonlin. (Cons. II)	15.43	19.01	$-1.17 < f_{\rm NL} < 39.43$	$-19.19 < f_{\rm NL} < 63.56$	35.6
BASS+MzLS	Nonlin. (Cons. II+nStar)	13.12	15.39	$-4.59 < f_{\rm NL} < 35.56$	$-24.88 < f_{\rm NL} < 59.31$	34.7
BASS+MzLS	Nonlin. (All Maps+nStar)	−3.73	−6.34	$-27.11 < f_{\rm NL} < 13.75$	$-47.44 < f_{\rm NL} < 33.94$	36.8
BASS+MzLS (imag. cut)	Nonlin. (Cons. II)	25.03	29.12	$6.16 < f_{\rm NL} < 52.44$	$-14.22 < f_{\rm NL} < 80.54$	36.2
BASS+MzLS (comp. cut)	Nonlin. (Cons. II)	16.99	20.90	$0.26 < f_{\rm NL} < 41.76$	$-18.30 < f_{\rm NL} < 67.12$	35.8
DECaLS North	Nonlin. (Cons. II)	41.02	44.89	$23.33 < f_{\rm NL} < 66.78$	$4.96 < f_{\rm NL} < 93.02$	41.1
DECaLS North	Nonlin. (Cons. II+CALIBZ+HI)	55.46	60.44	$36.78 < f_{\rm NL} < 84.05$	$17.86 < f_{\rm NL} < 112.81$	38.4
DECaLS North	Nonlin. (Cons. II+nStar)	31.45	34.78	$14.14 < f_{\rm NL} < 55.79$	$-5.81 < f_{\rm NL} < 80.80$	41.2
DECaLS North	Nonlin. (All Maps+nStar)	0.81	−5.68	$-29.73 < f_{\rm NL} < 16.71$	$-53.15 < f_{\rm NL} < 36.19$	45.1
DECaLS North + islands	Nonlin. (Cons. II)	41.05	44.82	$23.58 < f_{\rm NL} < 66.08$	$6.40 < f_{\rm NL} < 91.42$	40.7
DECaLS North (imag. cut)	Nonlin. (Cons. II)	43.27	48.39	$24.60 < f_{\rm NL} < 72.50$	$4.71 < f_{\rm NL} < 101.42$	35.1
DECaLS North (comp. cut)	Nonlin. (Cons. II)	40.55	44.63	$22.41 < f_{\rm NL} < 67.11$	$3.95 < f_{\rm NL} < 94.06$	41.4
DECaLS South	Nonlin. (Cons. II)	31.24	33.21	$14.89 < f_{\rm NL} < 52.40$	$-5.11 < f_{\rm NL} < 74.35$	30.2
DECaLS South	Nonlin. (Cons. II+CALIBZ+HI)	33.79	37.50	$17.71 < f_{\rm NL} < 57.42$	$-0.31 < f_{\rm NL} < 80.94$	30.8
DECaLS South	Nonlin. (Cons. II+nStar)	14.34	6.28	$-21.19 < f_{\rm NL} < 30.01$	$-53.63 < f_{\rm NL} < 49.51$	31.9
DECaLS South	Nonlin. (All Maps+nStar)	−36.76	−32.01	$-49.38 < f_{\rm NL} < -13.61$	$-65.26 < f_{\rm NL} < 7.52$	31.5
DECaLS South + DEC < −30	Nonlin. (Cons. II)	43.79	46.79	$30.16 < f_{\rm NL} < 63.41$	$16.38 < f_{\rm NL} < 82.72$	23.8
DECaLS South (imag. cut)	Nonlin. (Cons. II)	26.47	23.36	$3.18 < f_{\rm NL} < 47.84$	$-57.69 < f_{\rm NL} < 71.39$	30.0
DECaLS South (comp. cut)	Nonlin. (Cons. II)	29.62	31.76	$13.00 < f_{\rm NL} < 51.58$	$-9.78 < f_{\rm NL} < 74.28$	29.7

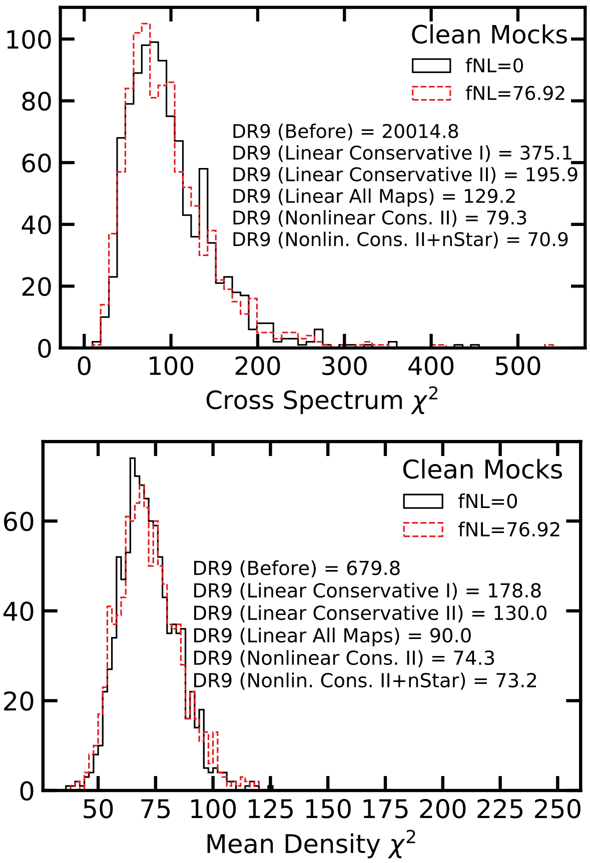

Figure 7. Left: Cross power spectrum χ^2 diagnostic. Right: Mean density contrast diagnostic. The values observed in DR9 before and after linear and nonlinear treatments are quoted and the histograms are constructed from 1000 realizations of clean mocks with $f_{\rm NL}$ = 0 and 100.

Gaia Collaboration et al., 2018, A&A, 616, A1
Gorski K. M., Hivon E., Banday A. J., Wandelt B. D., Hansen F. K., Reinecke M., Bartelmann M., 2005, The Astrophysical Journal, 622, 759
Ho S., et al., 2015, J. Cosmology Astropart. Phys., 2015, 040
Komatsu E., Spergel D. N., 2001, Physical Review D, 63, 063002
Myers A. D., et al., 2022, arXiv e-prints, p. arXiv:2208.08518
Pullen A. R., Hirata C. M., 2013, Publications of the Astronomical Society of the Pacific, 125, 705
Schlegel D. J., Finkbeiner D. P., Davis M., 1998, The Astrophysical Journal, 500, 525
Schmittfull M., Seljak U., 2018, Phys. Rev. D, 97, 123540
Slosar A., Hirata C., Seljak U., Ho S., Padmanabhan N., 2008, Journal of Cosmology and Astroparticle Physics, 2008, 031
Weinberg D. H., Mortonson M. J., Eisenstein D. J., Hirata C., Riess A. G., Rozo E., 2013, Physics reports, 530, 87
Zhou R., et al., 2021, Monthly Notices of the Royal Astronomical Society, 501, 3309

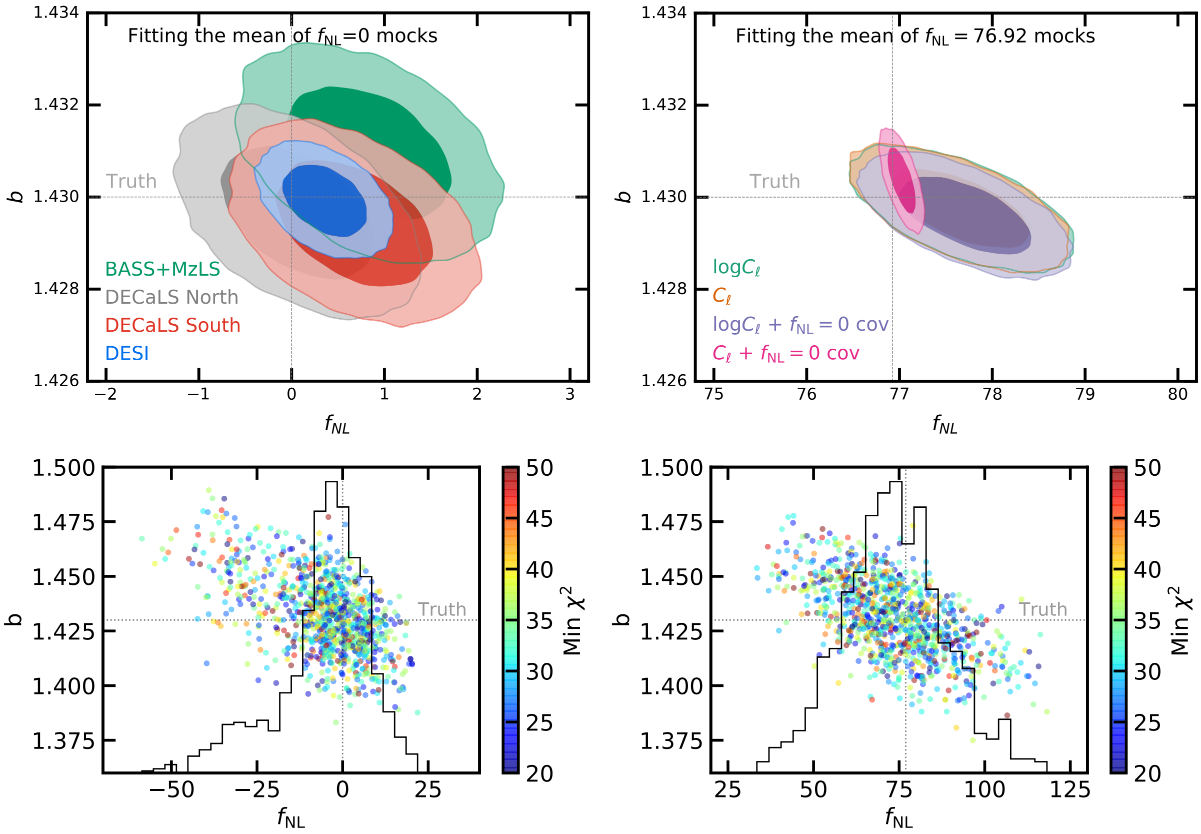

Figure 8. Top: 68% and 95% confidence contours for $f_{\rm NL} = 0$ (left) and 100 (right) mocks. Using the $\log C_\ell$ fitting yield constraints that are insensitive to the covariance used. Bottom: best fit estimates from fitting 1000 lognormal mocks with $f_{\rm NL} = 0$ (left) and 100 (right) in the DESI footprint. The truth values are represented by vertical and horizontal lines.

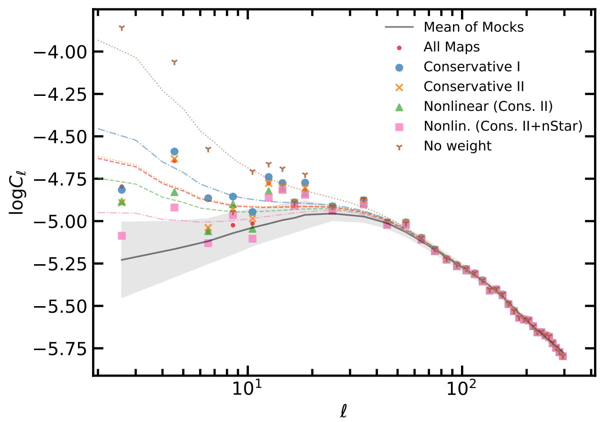

Figure 9. Measured power spectrum of the DR9 LRG sample before and after correcting for systematics with their corresponding best fit theory predictions. The shade represents 1σ error constructed from the $f_{\rm NL} = 0$ mocks.

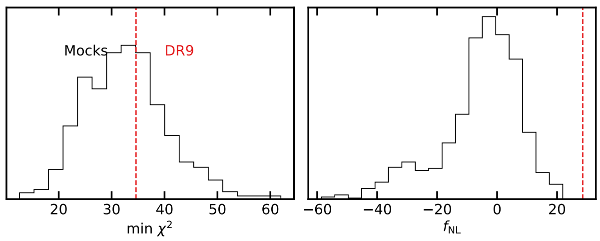

Figure 10. Best fit χ^2 and $f_{\rm NL}$ from fitting mocks (histograms) and DR9 (vertical line).

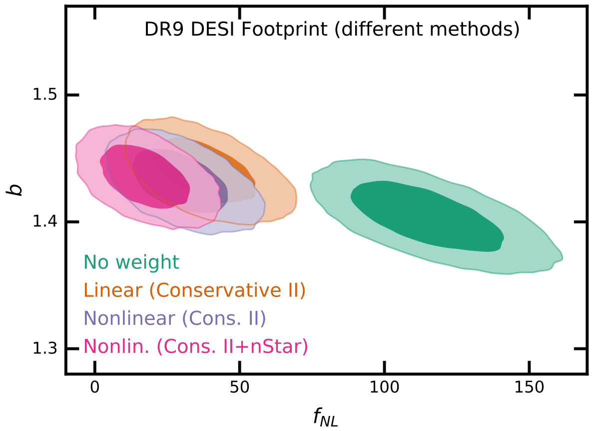

Figure 11. DR9 constraints. DESI footprint before and after applying various cleaning methods.

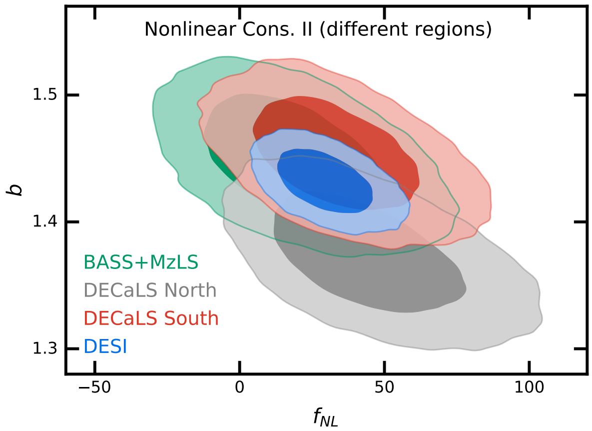

Figure 12. DR9 constraints. Each individual imaging survey versus the whole DESI footprint.

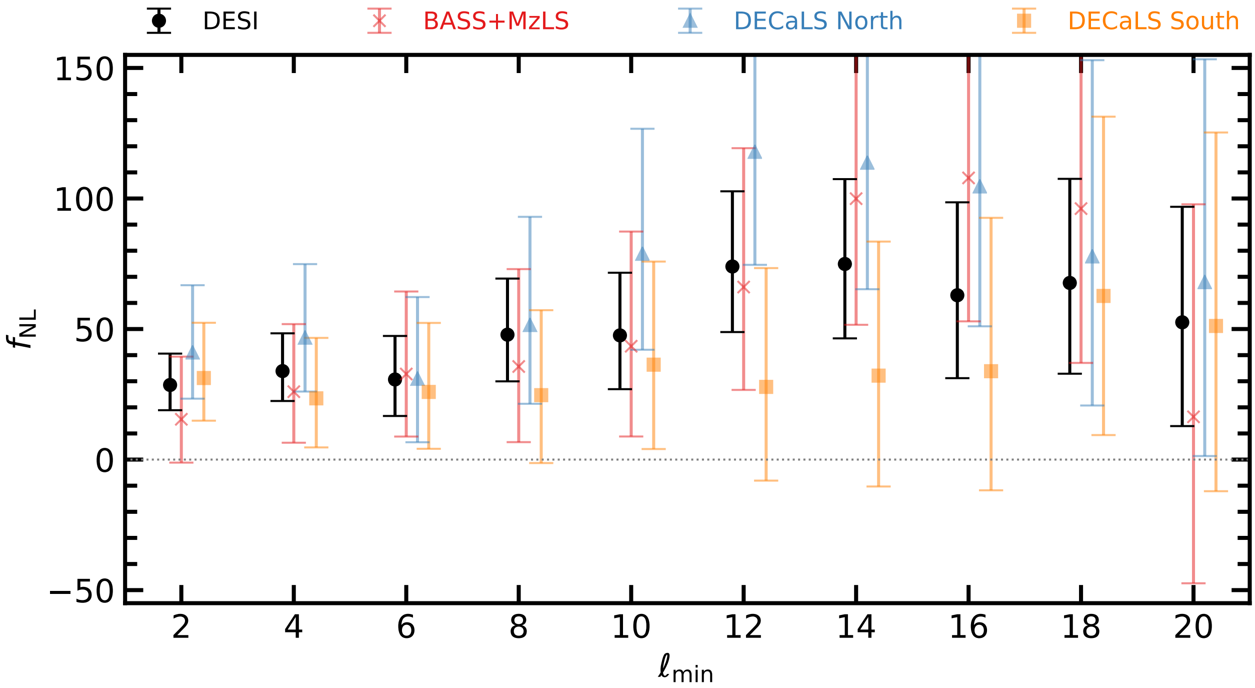

Figure 13. DR9 Constraints. Mean estimates of $f_{\rm NL}$ and its 65% and 95% errorbars after changing the lowest ℓ mode used in fitting.

APPENDIX A: REDSHIFT DISTRIBUTION

Redshift distribution of LRGs is constructed from the DESI SV data release of Denali with the same selection. The fiducial distribution only covers the redshift range from 0.2 to 1.35. Below we test the impact of LRG dN/dz on the angular power spectrum.

APPENDIX B: SCALE DEPENDENCE SYSTEMATICS

The default modes used in calculating the cross spectrum χ^2 diagnostic range for $2 \leq \ell < 20$. Here we further test the stability of our results by extending the highest mode out to $\ell = 100$ or fluctuations over scales as small as 1.8 degrees.

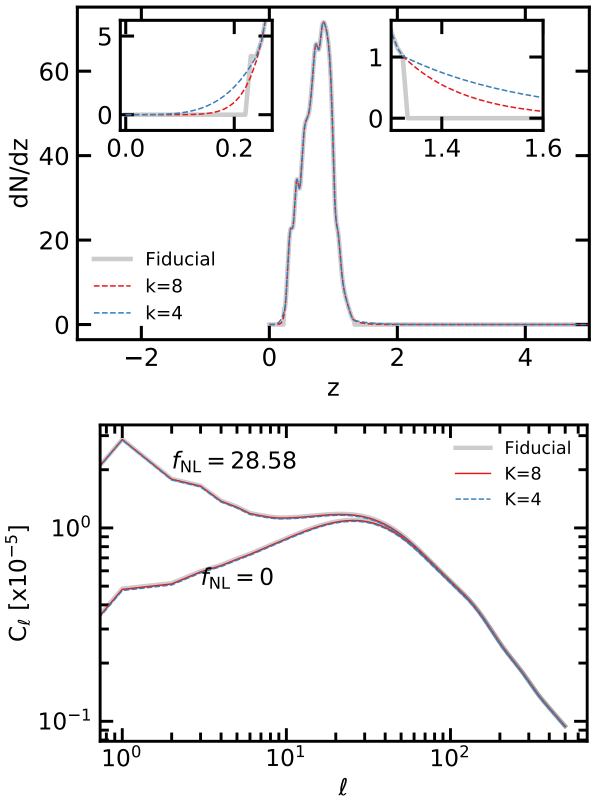

Figure A1. Top: Redshift distribution of LRGs. Bottom: Power spectrum given various dN/dz treatments for two arbitrary $f_{\rm NL}$ values.

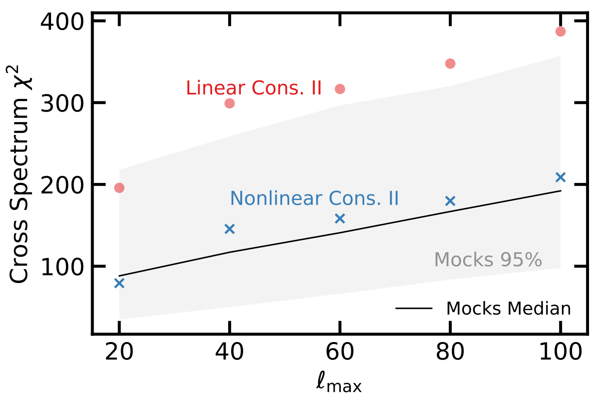

Figure B1. Cross Spectrum χ^2 as a function of the highest mode $\ell_{\rm max}$. The lowest mode is $\ell_{\rm min} = 2$.

This paper has been typeset from a TEX/LATEX file prepared by the author.